SCANNING TRANSMISSION ELECTRON MICROSCOPY (STEM) OF RUDDLESDEN-POPPER FAULTS IN NONSTOICHIOMETRIC CaTiO₃[†]

Miran Čeh

"Jožef Stefan" Institute, Ceramics Department, Jamova 39, Ljubljana, Slovenia

[†]This paper is dedicated to the late Professor Dr. Drago Kolar

Abstract

Oxide-rich planar faults with a rock-salt-type structure in perovskite grains are the prevailing type of planar defects in polycrystalline AO-doped $CaTiO_3$ (A=Ca,Sr,Ba). These so-called Ruddlesden-Popper (RP) faults form random network structures or ordered polytypes and polytypoids, depending on the processing parameters. The ordering of RP faults was observed by various high-resolution STEM imaging techniques. The local chemical composition was investigated by energy-dispersive X-ray spectrometry (EDXS) and electron energy-loss spectrometry (EELS). The achieved point-to-point resolution in bright-field (BF) and high-angle annular dark-field (HAADF) STEM imaging was below 0.27 nm. In Z-contrast imaging, it was possible to resolve 15% of the difference in the average atomic number (Z) between two adjacent atomic columns. Chemical analysis showed that Sr and Ba preferentially substitute for Ca in the $CaTiO_3$ lattice, thus forming a solid solution of $(Ca_{1-x}Sr_x)TiO_3$ and $(Ca_{1-x}Ba_x)TiO_3$. The excess Ca ions form single or ordered CaO-rich planar faults in the host solid-solution phase. Sr and Ba do not substitute for Ca on the sites at the fault. The polytypoids are comprised of a sequence of single CaO faults followed by a different number of $(Ca_{1-x}Sr_x)TiO_3$ or $(Ca_{1-x}Ba_x)TiO_3$ perovskite layers.

Introduction

The scanning transmission electron microscope (STEM) has significantly improved imaging and analytical capabilities in materials investigations. The basic concept of a STEM is to combine the performances of a transmission electron microscope (TEM), scanning electron microscope (SEM) and electron microprobe (EPMA).[1,2] There are two different types of STEM. The first is the so-called dedicated scanning transmission electron microscope (DSTEM), which generally uses a cold field-emission electron gun (FEG) housed in an ultra-high-vacuum system. The alternative is a conventional TEM equipped with a scanning unit that controls the beam movement across the sample. Such a microscope is referred to as a TEM(S) or TEM/STEM. However, initially these microscopes could not be compared in terms of performance

with a dedicated STEM, mainly due to a large beam size, a consequence of a thermoionic electron source. It was not until TEM(S)s were fitted with a field-emission gun source that they became comparable in performance with dedicated STEMs. In fact, one of the major advantages of these FEG TEM(S) over dedicated STEMs is that they unite the TEM and STEM concept in one instrument. One can therefore perform high-resolution transmission electron microscopy (HRTEM) and analytical electron microscopy (AEM) on the same sample in the same instrument. The basic mode of a STEM involves an extremely fine probe, usually less than 0.5 nm in diameter, being scanned across the thin foil specimen. The electrons that pass through the sample and are scattered either elastically or inelastically, can be collected by a bright-field (BF), annular dark-field (ADF) or high-angle annular dark-field (HAADF) STEM detector. These different STEM detectors convert the number of detected electrons into a suitable video signal to modulate the intensity of the beam in a cathode-ray-tube monitor. The X-ray excited in the sample by the high-energy electrons can be analyzed by energy-dispersive X-ray spectrometry (EDXS), producing qualitative or quantitative chemical nanoanalysis of the analyzed region. Finally, an electron energy-loss spectrometer (EELS) can differentiate the energies of the passing electrons. The obtained EEL spectra can provide information on the qualitative and quantitative chemical composition and the dielectric properties of the material.

The scanning transmission electron microscope (STEM) makes possible a large variety of imaging and analytical techniques not previously combined in a single instrument. The aim of this paper is to show the possibilities for ceramic materials investigations using scanning transmission electron microscopy, which will be illustrated by the results of imaging and chemical analysis of Ruddlesden-Popper (RP) faults in AO-doped $CaTiO_3$ (A=Ca,Sr,Ba). Bright-field (BF), annular dark-field (ADF) and high-angle annular dark-field (HAADF) detectors were used for imaging, while the local chemistry of planar faults, polytypes and polytypoids has been investigated by spatially resolved energy-dispersive X-ray spectrometry (EDXS) and electron energy-loss spectrometry (EELS).

Ruddlesden-Popper faults in ATiO$_3$ perovskites (A=Ca,Sr,Ba)

It is known that some titanates with the ATiO$_3$ perovskite structure compensate for nonstoichiometry (A/Ti>1.00) by forming of isolated or ordered planar faults. This phenomenon was observed in the SrTiO$_3$-SrO system,[3] the CaTiO$_3$-CaO system[4] and also in some mixed perovskites like SrO-doped CaTiO$_3$.[5]

An observation common to all these systems is that at a relatively small deviation from stoichiometry (A/Ti<1.05) and sintering temperatures <1400°C, the AO-excess is compensated for by the formation of random networks of isolated planar faults, which run parallel to the {100} lattice planes of the perovskite. A single planar fault has a rock-salt-type structure and is coherently intergrown with the ATiO$_3$ perovskite matrix. Across the fault, A and Ti cations in the neighboring perovskite blocks are brought into the anti-phase position for the ½[110] of the perovksite lattice (Fig. 1.).[6] Structurally, such a fault can be regarded as an anti-phase boundary with a composition AO. This type of planar fault is also known as a Ruddlesden-Popper fault (RP), since it was first described by Ruddlesden and Popper as a structural layer within the Sr$_4$Ti$_3$O$_{10}$ phase.[7]

At sintering temperatures higher than 1450°C, polytypic RP phases with the general formula A$_{n+1}$Ti$_n$O$_{3n+1}$ can be formed according to different compositions in the ATiO$_3$-AO phase diagrams. These phases are structurally composed of a single RP fault, which is followed by **n** perovskite blocks (n=1,2,3). In the CaTiO$_3$-CaO system two polytypic phases are reported: Ca$_3$Ti$_2$O$_7$ (n=2) and Ca$_4$Ti$_3$O$_{10}$ (n=3).[8,9] Due to a different Ca/Ti ionic ratio, the phase Ca$_2$TiO$_4$ is not stable. Ca$_3$Ti$_2$O$_7$ and Ca$_4$Ti$_3$O$_{10}$ consist of coherent intergrowths of **n** perovskite blocks with a single CaO layer having a distorted rock-salt configuration.[10] In both structures the TiO$_6$ octahedra are tilted and distorted in a fashion similar to that in CaTiO$_3$. In Ca$_4$Ti$_3$O$_{10}$ there are two distinct types of TiO$_6$ octahedra, those in the middle of the perovskite blocks (type I) and those at the edges of the blocks (type II), i.e. at the CaO layers (Fig. 1.). The mean Ca-O bond lengths in Ca$_4$Ti$_3$O$_{10}$ indicate that there are two distinct Ca sites in the polytypic structure, larger Ca$_I$ sites in the middle of CaTiO$_3$ blocks and smaller Ca$_{II}$ sites in the CaO layers. In the SrTiO$_3$-SrO system three polytypic phases are known: Sr$_2$TiO$_4$ (n=1), Sr$_3$Ti$_2$O$_7$ (n=2) and Sr$_4$Ti$_3$O$_{10}$ (n=3).[11-14] Again, the Sr$_2$TiO$_4$ phase can be described as the ordered
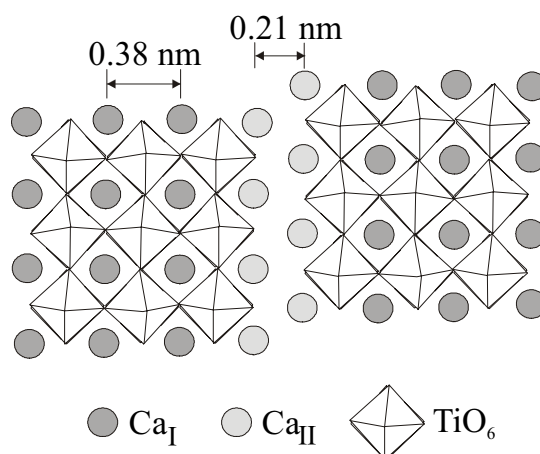
Figure 1. [001] view of a single RP-fault structure shows the anti-phase position of Ca and Ti atoms across the boundary for the ½[110] of the perovksite lattice.

sequence of a single SrO planar fault and a single $SrTiO_3$ perovskite block, while the phase $Sr_4Ti_3O_{10}$ is a sequence of one planar fault and three perovskite layers. These RP phases are completely ordered only when the exact stoichiometry is achieved. For the $Sr_4Ti_3O_{10}$ phase, the atomic Sr/Ti ratio should be 1.33. Finally, in the $BaTiO_3$-BaO system, the so called orthotitanate Ba_2TiO_4 phase is not a polytypic phase, since its structure cannot be described as a sequence of BaO layers and $BaTiO_3$ perovskite blocks. Nevertheless, very recent investigations have shown that isolated RP planar faults were also observed in BaO-doped $BaTiO_3$ thin films.[15]

When we apply small deviations from stoichiometry in AO-doped $CaTiO_3$ and $SrTiO_3$ (A/Ti<1.05) and sintering temperatures between 1450°C and 1550°C, we encounter a situation where we observe slabs of more-or-less ordered polytypic phases embedded in the perovskite $CaTiO_3$ and $SrTiO_3$ matrix. The resulting microstructure consists of composite-like $CaTiO_3$ and $SrTiO_3$ grains with polytypic slabs intersecting the grains. Grains with an embedded polytypic phase possess a highly anisotropic shape due to the preferential and faster growth of polytypic lamella compared to the surrounding $CaTiO_3$ and $SrTiO_3$ grains. This phenomenon was observed in CaO-doped $CaTiO_3$,[4] BaO-doped $CaTiO_3$[16] and recently also in SrO-doped $SrTiO_3$.[17]

When SrO or BaO are added to $CaTiO_3$, the mechanism of their incorporation bears a close resemblance to that of CaO into $CaTiO_3$.[18] When sintering $CaTiO_3$ with SrO or BaO at temperatures as high as 1550°C, ordered structures of the $(Ca_xSr_{1-x})_{n+1}Ti_nO_{3n+1}$ or $(Ca_xBa_{1-x})_{n+1}Ti_nO_{3n+1}$ polytypoidic homologous series are formed.

However, the distribution of Sr and/or Ba in polytypoidic structures was not known. Crystallographic studies of the $Ca_{3.6}Sr_{0.4}Ti_3O_{10}$ phase employing neutron diffraction and CBED[10] indicated that the addition of Sr had a significant influence on the polytypoid structure and that larger Sr atoms substituted preferentially on Ca_I sites, within the perovskite layers, while the Ca_{II} sites remained fully Ca occupied. However, up to now no in-situ chemical analysis was performed to confirm these results. Since single planar faults are, on average, 0.2 nm wide, highly spatially resolved analytical electron microscopy is needed to perform such chemical analysis.

Experimental procedures and methods

Analytical-grade starting materials were used for the preparation of samples. CaO, SrO and BaO were added to $CaTiO_3$ in the form of carbonates. The mixtures of $CaTiO_3$ and carbonates equivalent up to 25 mol% of AO, were uniaxially pressed into pellets in a steel die, and sintered in air at temperatures from 1350 to 1550 °C from 1 to 12 hours.

Thin foil specimens for transmission electron microscopy observations were prepared by ion-beam milling using argon ions at 4kV. Specimens were examined in a dedicated scanning transmission electron microscope STEM (HB 501, Vacuum Generators) and in a transmission electron microscope (JEM-2010F, Jeol). The dedicated STEM was fitted with a cold field-emission gun, and equipped with a parallel EEL spectrometer (Gatan 666) and a thin-window Ge EDX detector (Noran). The JEM-2010F was equipped with a Schottky-type field-emission gun and fitted with a scanning image observation system with bright-field (BF), annular dark-field (ADF) and high-angle annular dark-field (HAADF) scanning transmission electron detector. The inner and outer annular angles for the HAADF detector were 50 mrad and 110 mrad, respectively. The estimated beam size for high-resolution STEM imaging was less than 0.3 nm. Chemical analysis was performed with an X-ray energy-dispersive spectrometer (Oxford Instruments, LINK ISIS 300) and a parallel electron energy-loss spectrometer (Gatan, PEELS 766).

EDX spectra were acquired from points, lines and framescans of different dimensions from 100 to 300 s. A modified Kramers´ law[19] was used to model the background and the Cliff-Lorimer[20] equation was used to quantify the EDX spectra. The k-factors were determined experimentally from EDX spectra taken from pure compounds of $Ca_4Ti_3O_{10}$ and $SrTiO_3$[18]. No correction for the absorption of CaK_α, TiK_α and SrK_α lines was used since the EDX spectra were acquired from sufficiently thin regions of the foils. The interfacial coverage Γ (atoms/nm^2) was determined from framescans via the spatial difference method.[21]

The acquisition and processing of EEL spectra was controlled by a custom function incorporated into the EL/P software (Gatan). The EEL spectra were obtained in two different ways: from framescans, where the electron beam was scanning over an area to acquire one spectrum, or from linescans, where a group of EEL spectra were acquired while the beam was scanning a line across the specimen. A typical acquisition time for each spectrum during a linescan was 2 to 3 s. The EEL spectra for the planar faults were extracted from framescans or linescans by the spatial difference method.[22,23]

Results and discussion

Bright-field (BF) and dark-field (DF) STEM imaging

Experimental high-resolution BF and DF STEM images of isolated planar faults and ordered polytypoidic sequences in a BaO-doped $CaTiO_3$ crystal are shown in figure 2. Similar images were obtained for CaO- and SrO-doped $CaTiO_3$. The BF image is comprised of forward-scattered electrons and most of the inelastically scattered electrons in the transmitted beam. The information from such an image is quite similar to that of a BF TEM image. On the other hand, the ADF detector collects most of the elastically scattered electrons, while the transmitted central beam is not detected. Since the aberration effects of the lenses are more seriously pronounced for off-axis rays, the resolution of the DF image taken by an ADF detector is usually worse than the resolution of the corresponding BF image. The RP faults in both BF images (Fig. 2a,c) are visible as straight white lines. Different distances between the RP faults in figure 2a indicate that the sample was processed at a lower temperature. The ordered sequences

of the RP faults in figure 2c correspond to the $(Ca_{1-x}Ba_x)_4Ti_3O_{10}$ polytypoidic phase. The atomic columns in the perovskite matrix are also resolved in the BF image in figure 2a despite
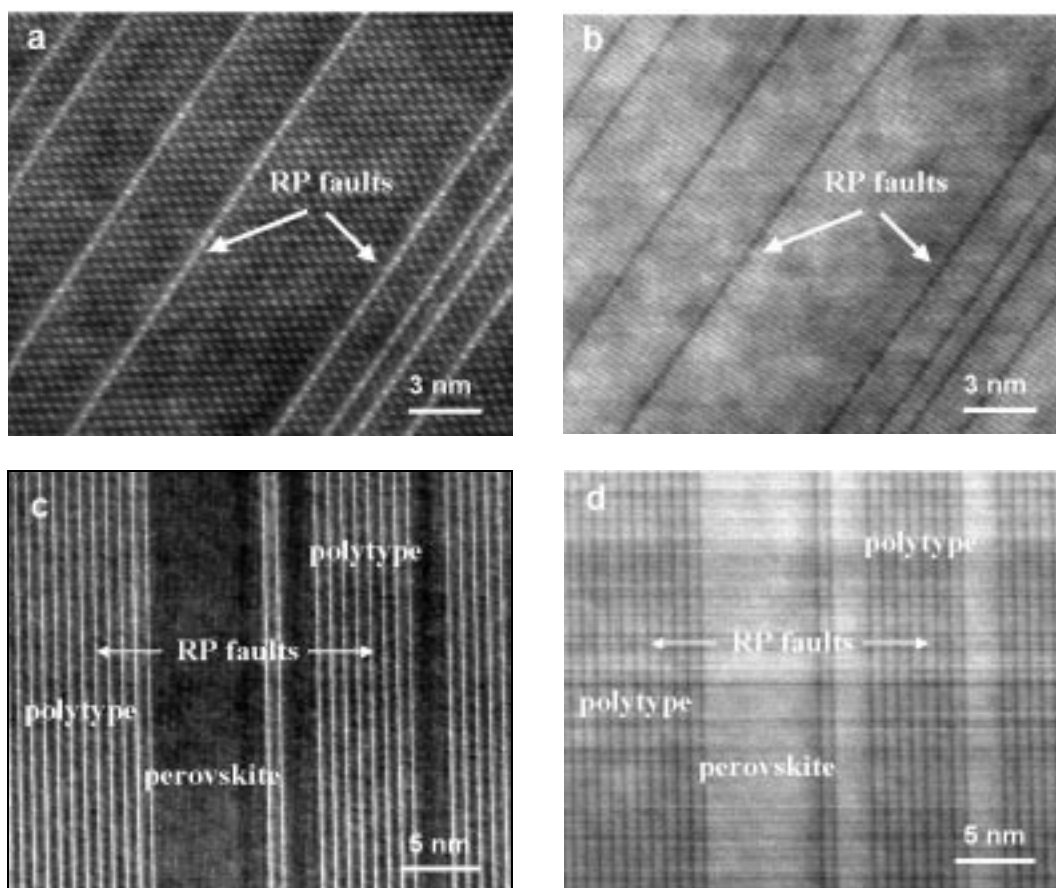

Figure 2. Bright-field (BF) and dark-field (DF) images of isolated RP faults and ordered RP polytypoidic phase in BaO-doped $CaTiO_3$ taken at different magnifications. BF images (a,c) possess better resolution than DF images (c,d). T=1540 °C, t=12 h.

the presence of some astigmatism, which is usually very difficult to correct in STEM images. With a probe diameter ~0.4 nm the best point-to-point resolution obtained with BF imaging was less than 0.27 nm, which is ½[110] of the perovskite unit cell. This is why the atomic columns at the RP fault that are 0.21 nm apart could not be resolved in figure 2a. In both DF images (Fig. 2b,d) the RP faults appear as dark lines, since the RP faults produce less high-angle scattered electrons. DF images have a lower resolution than the corresponding BF images. Since DF images are more sensitive to any deviations from the zone axis, the perovskite lattice image in figure 2b is resolved only in one direction.

High-angle annular dark-field imaging (HAADF) in STEM

DF images in a STEM are usually taken with an ADF detector that has an inner diameter less than 50 mrad. Such detector collects most of the elastically scattered electrons. If we increase the diameter of the hole in the detector then only high-angle scattered incoherent electrons are detected. Since high-angle scattering of the electrons strongly depends on the atomic number (Z) of the sample atoms, this type of STEM imaging is also named incoherent Z-contrast imaging.[24,25] The HAADF image can be interpreted directly without the need for preconceived structural models, this is in contrast to quantitative high-resolution transmission electron microscopy (HRTEM).[26]

Until recently, Z-contrast imaging has been exclusively performed in a dedicated STEM since incoherent imaging requires a very small probe, comparable in size to the lattice spacing of the material. New FEG transmission electron microscopes, however, are capable of performing similar, or even better, spatial resolution for Z-contrast imaging.[27-30] HAADF STEM experimental and filtered images of a single fault in the [001] perovskite zone axis in CaO-doped $CaTiO_3$ are shown in figures 3a,b. Filtering of
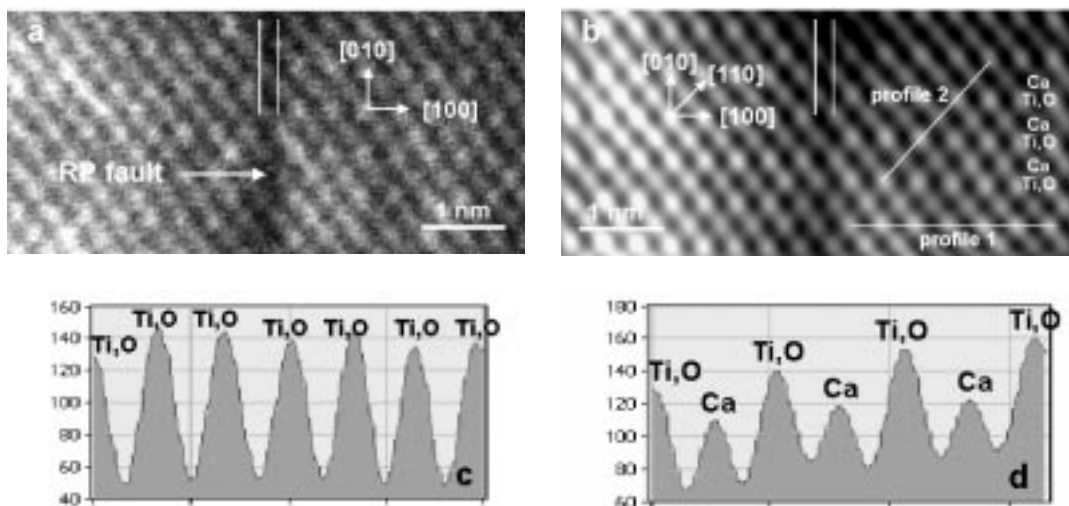

Figure 3. (a) Experimental HAADF STEM image of a RP planar fault in the [001] zone axis. A slight distortion in the vertical direction is observed. (b) Filtered HAADF image. The distance between two Ca atoms in the [100] direction is 0.38 nm and the distance between Ca and Ti atoms in the [110] direction is 0.27 nm. Atomic columns containing mixed Ti and O $(Z=(22^2+8^2)^{1/2}=23.4)$ are brighter than Ca atomic columns (Z=20). (c) Intensity profiles across Ti-O atomic columns (profile 1). (d) The variation in the profile intensity across atomic columns in [110] direction shows the difference in the contrast between Ti,O and Ca atomic columns.

the experimental image was performed by removal of the high spatial frequencies only. In the HAADF image the atomic columns of the perovskite lattice are resolved as white dots of different intensities, while the planar fault appears as a stripe of lower intensity. A slight distortion in the vertical direction of the image originates from the scanning. The distance between two Ca atoms in the [100] direction is 0.38 nm and the distance between Ca and Ti atoms in the [110] direction is 0.27 nm. A HAADF image of the perovskite matrix on both sides of the fault shows atomic columns containing Ca (Z=20) and the atomic columns containing alternating atoms of Ti and O ($Z=(22^2+8^2)^{1/2}=23.4$), which can be distinguished by their relative intensities (Fig. 3c,d.). The mixed atomic columns of Ti and O are brighter than the Ca columns. The low intensity of the two atomic columns along the fault unambiguously indicates that only Ca constitutes the anti-phase boundary, which is in agreement with the structural model of the fault.

Energy-dispersive X-ray spectrometry (EDXS)

In STEM mode, the very small spot size enables point analysis from nanosized regions. EDX spectra that were taken from the RP fault in the CaO-doped $CaTiO_3$ and the perovskite matrix clearly show that the Ca content at the RP fault is larger than the perovskite matrix (Fig. 4.). Since Ca is unique to either the planar fault or the perovskite matrix in CaO-doped $CaTiO_3$, SrO- and BaO-doped $CaTiO_3$ samples were prepared in order to study the distribution of Sr and Ba within the polytypoids and RP faults by EDX analysis. The results of a quantitative analysis of the polytypoidic phase in SrO-doped $CaTiO_3$ are shown in Table I. It is evident that the matrix is a perovskite solid solution with the formula $(Ca_{1-x}Sr_x)TiO_3$, while the ordered region corresponds to $(Ca_{1-x}Sr_x)_4Ti_3O_{10}$. These results, however, only give the overall composition and provide no information on the distribution of Sr within the polytype. To obtain this, we performed quantitative EDX analysis by the spatial difference method in order to determine the Ca excess at the RP faults of the polytypoid. The quantification of five spatial difference spectra between the perovskite matrix and the polytypoid regions showed an average Ca excess for the polytypoid of $\Gamma = 6.8\pm1.2$ Ca/nm², where Γ[21] is the area density of Ca
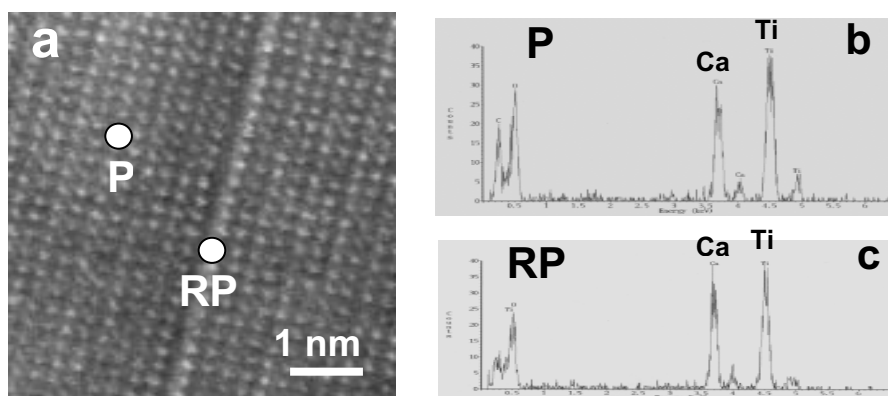
Figure 4. (a) BF STEM image of isolated RP fault with the corresponding EDX spectra taken from (b) the $CaTiO_3$ (P), and (c) from the RP fault showing a much larger concentration of Ca at the RP.

TABLE I.   Compositions of matrix and ordered regions for three different nominal compositions.

	9 mol% SrO	**12.5 mol% SrO**	**25 mol% SrO**
matrix	$(Ca_{0.90}Sr_{0.10})TiO_3$	$(Ca_{0.89}Sr_{0.13})TiO_3$	$(Ca_{0.70}Sr_{0.30})TiO_3$
polytypoid	$(Ca_{0.94}Sr_{0.07})_4Ti_3O_{10}$	$(Ca_{0.89}Sr_{0.09})_4Ti_3O_{10}$	$(Ca_{0.78}Sr_{0.22})_4Ti_3O_{10}$

atoms in the fault. This value agrees well with the calculated area density of Ca on the $\{100\}$ perovskite plane ($\Gamma=6.7$ Ca/nm^2), which indicates that the fault corresponds to one calcium monolayer.

Electron energy-loss spectrometry (EELS)

Since the acquisition time for an EEL spectrum is much shorter than the acquisition time for an EDX spectrum, due to a much better signal-to-noise ratio, EEL linescans and mappings are relatively easy to perform in a STEM. A region of the BaO-doped $CaTiO_3$ crystal containing five isolated RP faults is shown in figure 5. RP faults appear as dark lines in the image taken with the ADF detector. An EEL linescan across the RP faults shows an increase in the Ca concentration at the RP fault associated with a corresponding decrease in Ti concentration. For the detection of Ba, another linescan was recorded with a smaller beam shift and increased counting time per pixel (Fig. 6).

The concentration profile reveals a decrease in the Ba concentration at the RP fault, which is again a conformation that the atomic positions at the faults do not allow for
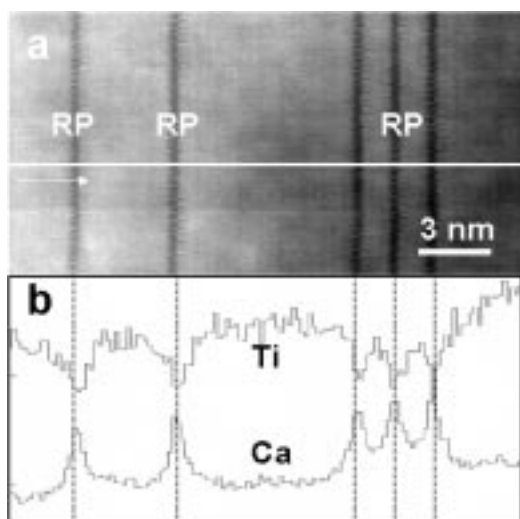
Figure 5. (a) DF image of five isolated RP faults in BaO-doped CaTiO$_3$. (b) Elemental profiles for Ca and Ti show increase in Ca concentration at the RP fault associated with a corresponding decrease in Ti concentration. The line of scan is marked in the DF image.
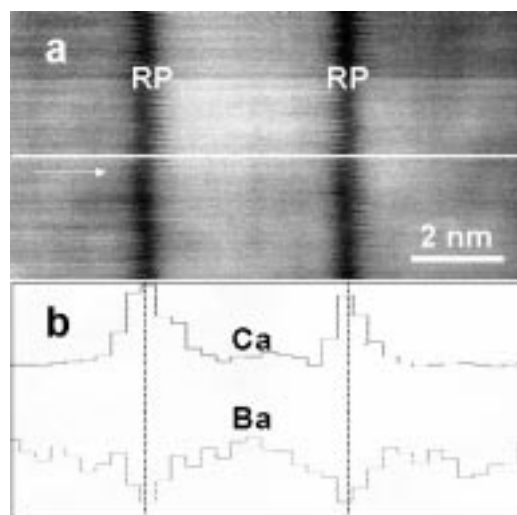
Figure 6. (a) DF image of two RP faults in BaO-doped CaTiO$_3$. (b) Elemental profiles for Ca and Ba were recorded with a smaller beam shift and increased counting time per pixel. The concentration profile reveals decrease of Ba at the RP fault. The line of scan is marked in the DF image.
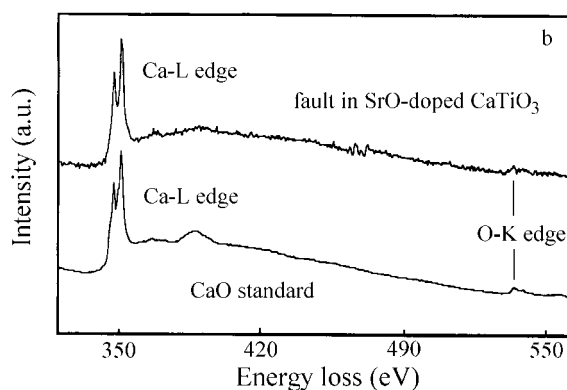
Figure 7. An average EEL spectrum for a RP fault and an EEL spectrum acquired from pure CaO standard. The comparison of both spectra indicates that RP fault is comprised of Ca ions only.

larger ions such as Ba and Sr. Since it is very difficult to detect small concentrations of Sr by EELS, due to the nature of the SrL and SrM edges, a spatial difference approach was used to determine the content of Sr at the RP fault. The EEL spectra obtained from the region with no RP faults were subtracted from the EEL spectra acquired from the

region with RP faults, yielding the spectrum of the RP fault only.[18] The comparison between the EEL spectra for the RP fault and the CaO standard shows that the two spectra are almost identical (Fig. 7.). In the spectrum from the fault, the Ca/O atomic ratio is 0.94±0.09, which agrees well with the CaO standard where the Ca/O is 1.

Conclusions

The presented results on imaging and the chemical analysis of isolated and ordered RP faults in AO-doped $CaTiO_3$ (A=Ca,Sr,Ba) have clearly demonstrated the usefulness and unique capabilities of a scanning transmission electron microscope (STEM) in materials investigations. BF, DF and HAADF imaging showed that RP faults form random networks, or highly ordered polytypic and polytypoidic structures within a perovskite matrix, depending on the processing parameters. The achieved point-to-point resolution in BF and HAADF STEM imaging was better than 0.27 nm. In Z-contrast HAADF imaging it was also possible to resolve ~15% of the difference in the average atomic number (Z) between two adjacent atomic columns. Spatially resolved EDXS and EELS provided results on the chemical composition of the investigated polytypes, polytypoids and the perovskite matrix. With the spatial difference method the composition of a single fault was determined. Based on the results it was shown that Sr and Ba do not substitute for Ca on the atomic positions at the fault (type II sites) but enter into Ca sites in the perovskite (type I sites), which leads to the formation of $(Ca_{1-x}Sr_x)TiO_3$ and $(Ca_{1-x}Ba_x)TiO_3$ solid solutions. Consequently, the polytypoidic $(Ca_{1-x}Sr_x)_4Ti_3O_{10}$ and $(Ca_{1-x}Ba_x)_4Ti_3O_{10}$ phases can be described as a sequence of a single CaO fault which is followed by three layers of either $(Ca_{1-x}Sr_x)TiO_3$ or $(Ca_{1-x}Ba_x)TiO_3$.

Acknowledgements

Science and Sport for the research at the Max-Planck-Institut für Metallforschung in Stuttgart, where analyses on VG HB501 dedicated STEM were performed.

References

1. D. C. Joy, A. D. Romig Jr., J. I. Goldstein, *Principles of Analytical Electron Microscopy*; Plenum Press, New York, 1986, pp 77-120.
2. D. B. Williams, C. B. Carter, *Transmission Electron Microscopy*; Plenum Press, New York, 1996, pp 349-366.
3. R. J. D. Tilley, *J. Solid. State Chem.* **1997**, 21, 293-301.
4. M. Čeh, D. Kolar, *J. Mater. Sci.* **1994**, 29, 6295-6300.
5. M. Čeh, V. Kraševec, D. Kolar, *J. Solid State Chem.* **1993**, 103, 263-268.
6. M. Čeh, A. Rečnik, *Microscopia Elettronica* **1993**, 12(2), 281-282.
7. S. N. Ruddlesden, P. Popper, *Acta Cryst.* **1958**, 11, 54-55.
8. R. C. Devries, R. Roy, E. F. Osborn, *J. Phys. Chem.* **1954**, 58, 1069-1073.
9. R. S. Roth, *J. Res. Natl. Bur. Standards* **1958**, 61, 437-440.
10. M. M. Elcombe, E. H. Kisi, K. D. Hawkins, T. J. White, P. Goodman, S. Matheson, *Acta Cryst.* **1991**, B47, 305-315.
11. G. J. McCarthy, W. B. White, R. Roy, *J. Am. Ceram. Soc.* **1969**, 52, 463-470.
12. K. R. Udayakumar, A. N. Cormack, *J. Am. Ceram. Soc.* **1988**, 71, C-469-471.
13. M. A. McCoy, R. W. Grimes, W. E. Lee, *Philos. Mag.* **1997**, A 75, 833-846.
14. K. Hawkins, T. J. White, *Philos. Trans. R. Soc. London* **1991**, A336, 541-569.
15. T. Suzuki, Y. Nishi, M. Fujimoto, *J. Am.* Ceram. Soc. **2000**, 83 (12), 3185-3195.
16. A. Rečnik, M. Čeh, D. Kolar, *J. European Ceram. Soc.*, in print
17. S. Šturm, A. Rečnik, C. Scheu, M. Čeh, *J. Mater. Res.* **2000**, 15, 1-9.
18. M. Čeh, H. Gu, H. Müllejans, A. Rečnik, *J. Mater. Res.* **1997**, 12, 2438-2446.
19. H. A. Kramer, *Phil. Mag.* **1923**, 46, 836-838.
20. G. Cliff, G. W. Lorimer, *J. Microsc.* **1975**, 103, 203-207.
21. J. A. S. Ikeda, Y. M. Chiang, A. J. Garratt-Reed, J. B. Vander Sande, *J. Am. Ceram. Soc.*, **1993**, 76, 2447-2459.
22. H. Müllejans, J. Bruley, *Ultramicroscopy*, **1994**, 53, 351-360.
23. H. Gu, M. Čeh, S. Stemmer, H. Müllejans, M. Rühle, *Ultramicroscopy*, **1995**, 59, 215-227.
24. S. J. Pennycook, D. E. Jesson, *Ultramicroscopy*, **1991**, 37, 14-38.
25. N. D. Browning, S. J. Pennycook, *J. Phys. D: Appl. Phys.* **1996**, 29, 1779-1798.
26. M. M. McGibbon, N. D. Browning, M. F. Chisholm, A. J. McGibbon, S. J. Pennycook, B. Ravikumar, V. P. Dravid, *Science*, **1994**, 266, 102-104.
27. M. Kawasaki, T. Yamazaki, T. Sato, K. Watanabe, M. Shijoiri, *Phil. Mag. A*, in press
28. M. Kawasaki, T. Yoshioka, S. Sato, T. Nomura, M. Shiojiri, *J. Electron Microsc.* **2000**, 49, 73-84.
29. T. Yamazaki, K. Watanabe, A. Rečnik, M. Čeh, M. Kawasaki, M. Shijoiri, *J. Electron Microsc.* **2000**, 49, 753-759.
30. E. M. James, N. D. Browning, A. W. Nicholls, M. Kawasaki, Y. Xin, S. Stemmer, *J. Electron Microsc.* **1998**, 47, 561-574.

Povzetek

Ruddlesden-Popperjeve (RP) ploskovne napake s strukturo kamene soli so glavna vrsta ploskovnih napak v CaTiO$_3$ s prebitnim oksidom AO (A=Ca,Sr,Ba). Odvisno od priprave vzorcev in temperature sintranja, tvorijo RP ploskovne napake poljubno mrežno strukturo oziroma urejene politipne in politipoidne faze. Urejanje RP ploskovnih napak smo

opazovali z različnimi tehnikami vrstične presevne elektronske mikroskopije (STEM). Lokalno kemijsko sestavo smo določevali z energijsko spektrometrijo rentgenskih žarkov (EDXS) in spektrometrijo izgub energije elektronov (EELS). Pri STEM opazovanju v svetlem polju (BF) in v temnem polju (HAADF) smo dosegli ločljivost med dvema točkama boljšo od 0.27 nm. Pri tehniki Z-kontrast opazovanja perovskitne strukture $CaTiO_3$ smo lahko ločili kontrast med dvema atomskima kolonama, ki sta se razlikovali za 15% povprečnega atomskega števila (Z). Rezultati kemijske analize so pokazali, da se Sr in Ba preferenčno vgrajujeta na mesta Ca v perovskitni strukturi, kar vodi do nastanka trdnih raztopin $(Ca_{1-x}Sr_x)TiO_3$ in $(Ca_{1-x}Ba_x)TiO_3$. Sr in Ba se ne vgrajujeta na atomska mesta Ca v RP ploskovni napaki. Strukturo politipoidnih faz lahko opišemo kot zaporedje ene CaO plasti in različnega števila perovskitnih plasti $(Ca_{1-x}Sr_x)TiO_3$ ali $(Ca_{1-x}Ba_x)TiO_3$.